ARTICLE

Real *versus* Measured Surface Potentials in Scanning Kelvin Probe Microscopy

Dimitri S. H. Charrier,[†,*] Martijn Kemerink,[†] Barry E. Smalbrugge,[‡] Tjibbe de Vries,[‡] and René A. J. Janssen[†]

[†]Applied Physics, Eindhoven University of Technology, P.O. Box 513, 5600 MB, Eindhoven, The Netherlands, and [‡]COBRA Research Institute, Eindhoven University of Technology, P.O. Box 513, 5600 MB, Eindhoven, The Netherlands

ABSTRACT Noncontact potentiometry or scanning Kelvin probe microscopy (SKPM) is a widely used technique to study charge injection and transport in (in)organic devices by measuring a laterally resolved local potential. This technique suffers from the significant drawback that experimentally obtained curves do not generally reflect the true potential profile in the device due to nonlocal coupling between the probing tip and the device. In this work, we quantitatively explain the experimental SKPM response and by doing so directly link theoretical device models to real observables. In particular, the model quantitatively explains the effects of the tip–sample distance and the dependence on the orientation of the probing tip with respect to the device.

KEYWORDS: scanning Kelvin probe microscopy · electrical characterization · capacitive coupling · numerical modeling · organic transistors

In recent years, the potential mapping on organic semiconductor devices has been steadily gaining momentum. Scanning Kelvin probe microscopy (SKPM) and electric force microscopy (EFM) both offer unique opportunities to measure local surface potentials with ~100 nm resolution on operational devices. Since the measured surface potential seems to reflect the actual potential in the active layer and this information is otherwise unattainable, these techniques are becoming more and more popular for characterizing physical aspects of organic thin film devices[1] such as charge transport in polymer transistors[2] and charge generation in organic solar cells.[3]

As a consequence, the resolution of the SKPM measurements is an important issue. Several experimental and theoretical studies have identified the tip-to-sample distance[4–14] and the tip radius[15,16] as the limiting parameters. Actually, the lateral resolution is affected by the capacitive coupling between the entire tip, including the apex, cone, and lever, and the device. Due to this complex geometry, the problem is three-dimensional, and so far, no predictive model has been reported in the literature. The two-dimensional simulations that have been reported[17–20] do not account for the asymmetric influence of the lever,[6,21] which causes the problem to become truly three-dimensional. We used a standard organic transistor layout without an active layer, see Figure 1, as a relevant test system to quantify the electrostatic tip–sample interaction. It appears that the measured potential profile between "source" and "drain" electrodes strongly depends on whether the tip is parallel or orthogonal to the channel. Moreover, only a fraction (from 50% to 90%) of the applied voltage is observed in measured potential traces. It would seem, therefore, that further investigations are needed to quantify and understand the non-negligible influence of the entire tip–sample interaction. This paper describes a numerical tool, enabling the quantitative prediction of the surface potential as measured by SKPM without the use of any fitting parameters.

The rest of this paper is organized as follows. In the first part, we will describe the principle of the surface potential measurements which allows us to show the experimental resolution problem in detail. In the second part, we will describe the three-dimensional SKPM simulations, and we will confront them with the measurements on the test devices.

RESULTS

Experimental SKPM Results. SKPM combines the classical Kelvin probe technique with atomic force microscopy (AFM). Ideally, SKPM probes the electrochemical potential of the sample under the tip apex, which in the case of a metallic tip and sample with work function χ_{tip} and χ_{sample}, respectively, is equivalent to a measurement of the contact potential difference $V_{cpd} = (\chi_{tip} - \chi_{sample})/e$, where e is the electron charge.

The SKPM measurements are performed on a commercial AFM system (Dimension 3100 connected to a Nanoscope IIIa control-

*Address correspondence to d.charrier@tue.nl.

Received for review August 24, 2007 and accepted March 07, 2008.

Published online March 20, 2008.
10.1021/nn700190t CCC: $40.75

© 2008 American Chemical Society

ler equipped with a Quadrex module, Veeco Instruments) using metallized cantilevers (OMCL-AC240TM, Olympus, resonant frequency ~70 kHz, spring constant ~2 N/m, lever thickness 2.8 μm, lever length 240 μm, lever width 30 μm). The tip height is 14 μm, and the tip radius is ~30 nm. Potential maps are taken in interleave mode in which the potential is measured at each scan line in a second pass at a predefined lift height Δz. An AC bias V_{ac} at frequency ω close to the AFM tip resonance frequency is applied between the tip and the sample, in combination with a DC voltage V_{dc}. The force along the z axis is given by $F_z = -(V^2/2)(dC/dz)$ with $V = V_{dc} + V_{ac}\sin(\omega t) - V_{cpd}$ where C is the entire capacity between the tip and the surface. By introducing the latter expression into the force expression, the force at the resonant frequency becomes $F_\omega = (dC/dz)V_{ac}(V_{cpd} - V_{dc})$. The force F_ω is nullified by setting $V_{cpd} = V_{dc}$ and does not depend on the resonant frequency ω which becomes a noninfluencing parameter. Strictly spoken, this is only valid for a metal/metal configuration of two infinite plates, and for the metal/semiconductor case, V_{cpd} is different and is extensively described by Hudlet *et al.*[22]

We performed SKPM measurements on bottom-contact bottom gate transistor substrates while applying a source-drain voltage of 10 V. Because of the absence of an active layer, the naively expected potential profile is a plateau at 0 V over the source and a plateau at 10 V over the drain, linked by a straight line in the channel, as indicated by the dotted line in Figure 1. The SKPM result obtained for $\Delta z = 0$ nm is shown in Figure 1. Wu *et al.*[23] remarked that due to the oscillation amplitude, $\Delta z = 0$ nm corresponds at a tip-to-sample distance around 30 nm. Clearly, several deviations from the expected behavior are visible. The potential profile is not constant over the electrodes; the highest curvature does not occur at the channel edge; and the full bias of 10 V is not visible. In the literature, several works showed the same behavior.[22,24–28] Moreover, depending on the tip-to-channel orientation (orthogonal or parallel), the surface potential is dramatically different. A second observation is the strong influence of the tip-to-sample distance, which was discussed before[4–14] as being a limiting parameter. Figure 2 shows a set of data for different Δz (0, 100, and 1000 nm). These observations have strong impact on the applicability of SKPM for the investigation of (organic) transistors and other devices, since the models to which the measured potential profiles are compared do not take these limitations into account. It should be emphasized that even for the smallest lift height the error is non-negligible, as witnessed by Figures 1 and 2. To overcome this problem, the raw data are often rescaled to the expected values,[29,30] although this is not common practice.[31,32] The rescaling procedure does not solve the problem for both mathematical and practical reasons and deletes part of the information. In our case, such rescaling does not remove the rounding in the experimental curves nor does it repair the geometry-induced asymmetry. To quantify these problems and to come to a workable link between device model and SKPM response, we developed a fully 3D SKPM modeling. The simulations discussed in the next sections excellently fit the experimental data, as shown by the continuous lines in Figures 1 and 2.

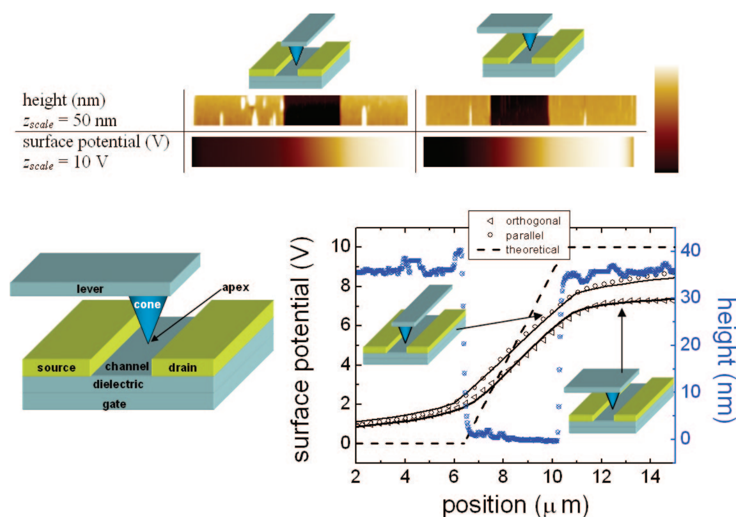

Figure 1. Top: table showing topography and surface potential measured on a test device in two different orientations, tip parallel to the channel and tip perpendicular to the channel. Bottom left: schematic view of the probe area. Bottom right: Potential profile as measured by SKPM. The symbols (lines) denote experimental data (numerical simulations), done at 0 nm lift height. The applied potential profile is shown as a dashed line. Note the difference in potential profile depending on the cantilever orientation. The insets show the tip and sample orientation. The blue dotted line shows a topography line section.

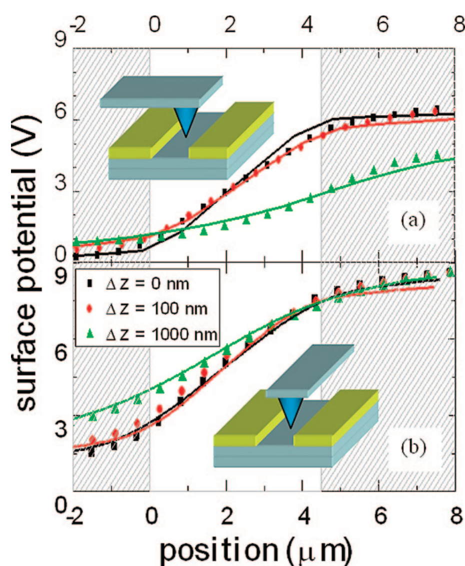

Figure 2. Experimental (symbols) and modeled (lines) surface potentials for three different tip–surface distances Δz over a 4.5 μm long channel. $\Delta z = 0$ nm (squares), 100 nm (circles), and 1000 nm (triangles). (a) With the tip orthogonal to the channel. (b) With the tip parallel to the channel. In both cases, the measured voltage difference is decreasing with the lift scan height. The insets show the tip and sample orientation.

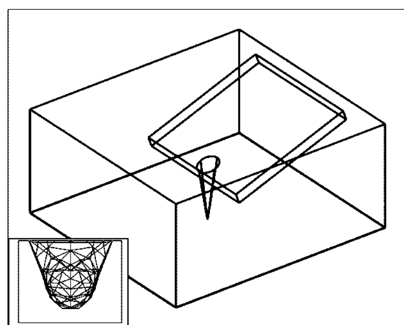

Figure 3. Three-dimensional drawing of the tip—consisting of the lever, cone, and apex—into a vacuum box which determines the calculation space. The box size is 50 µm × 65 µm (surface) × 25 µm (height). The drawn tip is not an exact replica of the tip used in the experiments, but all characteristic features (cone angle and height, apex radius, width, and tilt of the lever) are reproduced. The inset is a zoom on the tip meshing, showing that the apex is defined as a combination of tetrahedrons which can lead to a limitation in resolution (see text).

Simulation of SKPM. To simulate the SKPM technique, we used a commercial finite-element package which allows one to draw and subsequently simulate realistic tip and device shapes (see Figure 3 (a) and (b)). An additional organic layer, which would be present in an actual organic field effect transistor, can be easily added in a future work. A meshing procedure fills the entire space with tetrahedrons while conserving continuity at their interfaces and builds up all objects as compositions of tetrahedrons (see Figure 3 (b)). The discrete filling of tetrahedrons causes a limitation in resolution if the meshing density is low. The software tool used allows one to control the meshing in some detail, which is crucial for reducing the numerical scatter to an acceptable level. The issue of numerical noise is further addressed below in the discussion of Figure 5. It is important to point out that the model described above does not have any fitting parameters, *i.e.*, all parameters are known prior to the simulation.

Subsequently, the SKPM response V_{SKPM} is calculated as follows: for a given tip-to-sample distance and lateral tip position, the vertical force between the tip and the surface is calculated as a function of V_{dc}. The force F_z *versus* V_{dc} is a parabola as expected from simple electrostatics, of which the potential V_{SKPM} that is measured by SKPM is the maximum (see Figure 4).

Then, for each new geometry, the force between the tip and surface as a function of tip-to-sample distance is calculated. Figure 5 shows the force for both tip-to-channel orientations. The curves are not smooth since the meshing procedure creates a slightly different distribution of tetrahedrons after every change in geometry. However, once proper settings are found, a relatively smooth curve with few deviating points is obtained. In the subsequent calculation of lateral SKPM profiles, the particular tip-to-sample distances at which scatter occurs are avoided. To check if the simulated downward force is reasonable, a comparison with analytical expressions given in the literature for a system

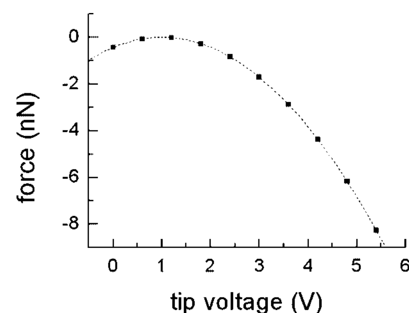

Figure 4. Vertical force between the probe (including the cone, apex, and cantilever) and the entire device *versus* bias applied to the probe. Since the SKPM technique nullifies this force, the voltage at the extreme of the parabola equals the SKPM output $V_{SKPM}(x)$. The calculation is done in the channel close to the source.

consisting of an apex plus a cone[16] is made. We find that both the order of magnitude and the behavior at small separation are similar, whereas the height dependence at larger separation is weaker in the present case because of the (almost constant) coupling of the relatively large lever to the sample, which is not present in the analytical expressions.

Figure 2 (a) and (b) shows the experimental and simulated surface potentials for three different lift scan heights, 0, 100, and 1000 nm, in the orthogonal and parallel configuration. Clearly, all characteristic features in the experimental traces like the nonconstant signal above the electrodes and the loss of resolution with increasing height are well reproduced by the calculations. Also, the dependence on tip-to-channel orientation is correctly described by the model. As anticipated, the (lack of) symmetry of the experimental situation with respect to the middle of the channel in the (anti) parallel situation results in (a)symmetric SKPM traces. Obviously, the real electrostatic potential profile is symmetric in both cases. We attribute the small differences between the experimental and modeling curves to slight differences between the modeled and true tip. In particular, the precise inclination of the cantilever and the exact shape of the cone are unknown.

Having established the model, it is worthwhile to briefly point out some "scaling" properties of SKPM

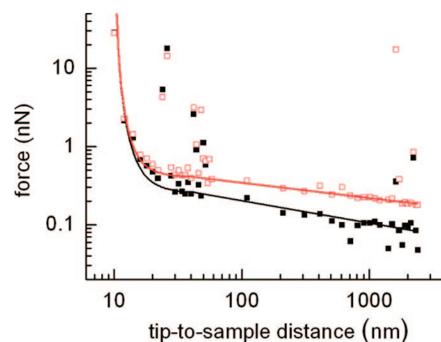

Figure 5. Vertical (downward) force between the tip and the surface *versus* their separating distance. The calculations were done in the middle of the channel. Empty squares (full squares) correspond to the tip orthogonal (parallel) to the channel. The thin lines are a guide to the eye.

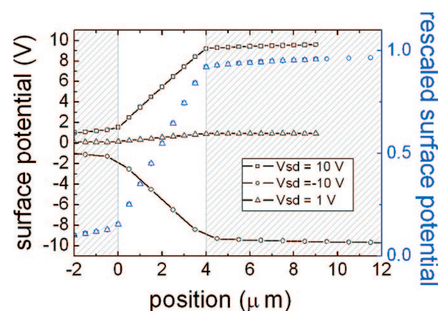

Figure 6. (a) Potential profiles for three different source-drain potentials V_{SD} = 10, 1, and −10 V (top to bottom). (b) as (a), after rescaling the curves in panel (a) by dividing them by the applied source-drain bias.

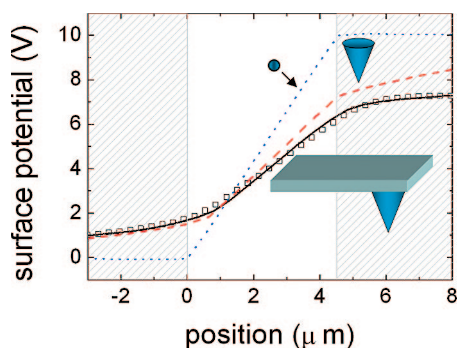

Figure 7. Experimental potential profile in the situation with the lever orthogonal to the channel (squares) and modeling for a full 3D tip (black line) containing the apex, cone, and lever. The red dashed line is the simulation for a probe consisting only of the cone + apex, the blue dotted line for a probe consisting of only an apex.

measurements. Figure 6 shows three different biasing configurations that are possible with the tip orthogonal to the channel. Electrostatically, these situations are equivalent. Therefore, provided that the shape of the potential distribution $V(x)$ is independent of the magnitude of the bias, as is the case in our test devices, one may anticipate that all SKPM curves can be rescaled to one "master curve" that only depends on the geometry. Obviously, the same holds for the tip parallel to the channel. For the simulations, this result implies that per geometry only one calculation is needed and that $V_{SKPM}(x)$ of configurations with different biases on the source and drain electrodes can be obtained by simple rescaling. Note, however, that in many "real" devices like FETs outside the linear regime, the shape of $V(x)$ is not independent of source-drain bias.

To qualitatively estimate the contribution of different tip parts, Figure 7 shows the experimental potential profile in the geometry with the lever orthogonal to the channel and three different modeling curves. The solid black line is calculated for the full 3D probe consisting of the apex, cone, and lever. Calculations for a probe consisting of the cone + apex (red dashed line) and only a single apex (blue dotted line) are also shown. A few comments can be given. As soon as the lever disappears to leave only the apex + cone, the full potential difference at the electrodes becomes 20% higher. Moreover, the nonsymmetric potential profile that is calculated with the full tip becomes symmetric upon removal of the lever, reflecting the increased symmetry of the "reduced" probes. Also, when the cone is removed from the calculation, the potential profile becomes virtually identical to the true surface potential. The minor deviations in the present calculation are due to the limited number of calculated lateral points. From a comparison of these three situations, it follows that the optimal geometry for a practical probe is one where (a) the cone is long—to reduce the coupling between the sample and the lever—and slender—to minimize the coupling between the sample and the cone itself—and (b) the lever is narrow—again to avoid undesired coupling to the sample. Moreover, to avoid asymmetry, the lever is preferably kept parallel to the channel.

CONCLUSIONS

Summarizing, we have shown that the potential profiles that are measured by scanning Kelvin probe Microscopy do not purely reflect the electrostatic potential under the tip apex but are strongly affected by the electrostatic coupling between the *entire* probe and the *entire* device, even at small tip–sample separation. We have developed a 3D numerical model that enables one to quantitatively predict the SKPM output from a known potential distribution and geometry. The model is successfully compared to SKPM measurements performed on relevant test devices.

MATERIALS AND METHODS

The used samples were typical bottom contact and bottom gate transistor substrates defined using UV lithography and lift-off, *i.e.*, a device structure that is commonly used in organic semiconductor research and technology. The structures were fabricated on n^+−Si wafers with a thick (1 μm) thermally grown SiO_2 oxide layer (ε_r = 3.9). The source and drain electrodes consisted of 25 nm Au on top of a 5 nm Ti adhesion layer and were shaped either as interdigitated fingers or as concentric rings, both with various *Width*/*Length* ratios. For the present work, no substantial differences between interdigitated and ring geometries were found.

Numerical simulations were performed using COMSOL 3.2b in combination with MatLab 7.1 running on a desktop PC with 2 GB of internal memory. In the simulations, the entire system was split into three blocks, being the tip containing a semispherical apex, a cone, and a parallelepiped lever, the surrounding vacuum block, and a block representing the substrate surface and contacts (Figure 3). Once the geometry was drawn, the subdomain settings had to be defined, the subdomains being blocks. The tip was defined as platinum, and the space around the tip was air. An organic layer, if present, was a dielectric layer defined with a dielectric constant ε_r. To simplify the geometry and avoid the need of remeshing for each lateral tip position, the electrodes were assumed to have zero height, so their potential can be analytically defined via boundary condition settings. The order of error of this assumption had not been strictly checked since the calculations would require a huge amount of memory which was out of our computational possibility. However, we expected that the error was confined to a narrow region with a width that was comparable to the electrode height, *i.e.*, a few tens of nanometers.

The boundary settings were a DC potential V_{dc} on the tip, continuity for all the interior boundaries, and electric insulation for the exterior boundaries. The surface potential $V_{cpd}(x)$ from which the SKPM response V_{SKPM} was to be determined was defined as a boundary condition for the potential of the bottom surface, using an equation function of coordinates (Oxyz). By defining the surface potential on top of the gate oxide, the underlying bulk layers, *i.e.*, the dielectric SiO_2 and gate n^+-Si, needed not to be defined anymore since the surface potential boundary condition contained their contribution and (by definition) screens everything underneath. Instead of moving the tip, which required remeshing and caused significant numerical noise, the channel was analytically moved along the *x* axis. Moreover, COMSOL offered the possibility to increase locally the meshing quality when the parameters by defaults gave a nonoptimized resolution between the apex and the surface. The "maximum element size" parameter specified the maximum allowed element size, which by default was 1/10th of the maximum distance in the geometry. The apex had a maximum element size equal to 0.09 in the COMSOL unit, corresponding to 18 nm. The "element growth rate" determined the maximum rate at which the element size can grow from a region with small elements to a region with larger elements. The value must be greater or equal to one. In our calculation, we took the element growth rate at 1.7.

Acknowledgment. The work of D.S.H.C. is made possible by a NanoNed grant (NanoNed is the Dutch nanotechnology initiative by the Ministry of Economic Affairs). We thank COBRA Research Institute for assistance with micropatterning.

REFERENCES AND NOTES

1. Palermo, S.; Palma, M.; Samorì, P. Electronic Characterization of Organic Thin Films by Kelvin Probe Force Microscopy. *Adv. Mater.* **2006**, *18*, 145–164.
2. Bürgi, L.; Richards, T.; Chiesa, M.; Friend, R. H.; Sirringhaus, H. A Microscopic View of Charge Transport in Polymer Transistors. *Synth. Met.* **2004**, *146*, 297–309.
3. Coffey, D. C.; Ginger, D. S. Time-Resolved Electrostatic Force Microscopy of Polymer Solar Cells. *Nat. Mater.* **2006**, *5*, 735–740.
4. Weng, Z.; Kaminsky, T.; Bridges, G. E.; Thomson, D. J. Resolution Enhancement in Probing of High-Speed Integrated Circuits Using Dynamic Electrostatic Force-Gradient Microscopy. *J. Vac. Sci. Technol. A* **2004**, *22*, 948–953.
5. Sacha, G. M.; Sáenz, J. J. Cantilever Effects on Electrostatic Force Gradient Microscopy. *Appl. Phys. Lett.* **2004**, *85*, 2610–2612.
6. Koley, G.; Spencer, G.; Bhangale, H. R. Cantilever Effects on the Measurement of Electrostatic Potentials by Scanning Kelvin Probe Microscopy. *Appl. Phys. Lett.* **2001**, *79*, 545–547.
7. Gil, A.; Colchero Gómez-Herrero, J.; Baró, A. M. Electrostatic Force Gradient Signal: Resolution Enhancement in Electrostatic Force Microscopy and Improved Kelvin Probe Microscopy. *Nanotechnology* **2003**, *14*, 332–340.
8. Takahashi, T.; Ono, S. Tip-to-Sample Distance Dependence of an Electrostatic Force in KFM Measurements. *Ultramicroscopy* **2004**, *100*, 287–292.
9. Belaidi, S.; Girard, P.; Leveque, G. Electrostatic Forces Acting on the Tip in Atomic Force Microscopy: Modelization and Comparison with Analytic Expressions. *J. Appl. Phys.* **1997**, *81*, 1023–1030.
10. Vatel, O.; Tanimoto, M. Kelvin Probe Force Microscopy for Potential Distribution Measurement of Semiconductor Devices. *J. Appl. Phys.* **1995**, *77*, 2358–2362.
11. Shikler, R.; Rosenwaks, Y. Measuring Minority-Carrier Diffusion Length Using a Kelvin Probe Force Microscope. *Appl. Surf. Sci.* **2000**, *157*, 11041–11046.
12. Hudlet, S.; Saint Jean, M.; Guthmann, C.; Berger, J. Evaluation of the Capacitive Force between an Atomic Force Microscopy Tip and a Metallic Surface. *Eur. Phys. J. B* **1998**, *2*, 5–10.
13. Foster, A. S.; Kantorovich, L. N.; Shluger, A. L. Tip and Surface Properties from the Distance Dependence of Tip–Surface Interactions. *Appl. Phys. A: Mater. Sci. Process.* **2001**, *72*, 59–62.
14. Bonaccurso, E.; Schönfeld, F.; Butt, H.-J. Electrostatic Forces Acting on Tip and Cantilever in Atomic Force Microscopy. *Phys. Rev. B* **2006**, *74*, 085413/1–8.
15. Sacha, G. M.; Verdaguer, A.; Martinez, J.; Sáenz, J. J.; Ogletree, D. F.; Salmeron, M. Effective Tip Radius in Electrostatic Force Microscopy. *Appl. Phys. Lett.* **2005**, *86*, 123101/1–3.
16. Argento, C.; French, R. H. Parametric Tip Model and Force–Distance Relation for Hamaker Constant Determination from Atomic Force Microscopy. *J. Appl. Phys.* **1996**, *80*, 6081–6090.
17. Tevaarwerk, E.; Keppel, D. G.; Rugheimer, P.; Lagally, M. G.; Eriksson, M. A. Quantitative Analysis of Electric Force Microscopy: The Role of Sample Geometry. *Rev. Sci. Instrum.* **2005**, *76*, 053707/1–5.
18. Jacobs, H. O.; Leuchtmann, P.; Homan, O. J.; Stemmer, A. Resolution and Contrast in Kelvin Probe Force Microscopy. *J. Appl. Phys.* **1998**, *84*, 1168–1173.
19. Gross, T. S.; Prindle, C. M.; Chamberlin, K.; bin Kamsah, N.; Wu, Y. Two-Dimensional, Electrostatic Finite Element Study of Tip–Substrate Interactions in Electric Force Microscopy of High Density Interconnect Structures. *Ultramicroscopy* **2001**, *87*, 147–154.
20. Belaidi, S.; Lebon, F.; Girard, P.; Leveque, G.; Pagano, S. Finite Element Simulations of the Resolution in Electrostatic Force Microscopy. *Appl. Phys. A: Mater. Sci. Process.* **1998**, *66*, 239–243.
21. Hochwitz, T.; Henning, A. K.; Levey, C.; Daghlian, C.; Slinkman, J. Capacitive Effects on Quantitative Dopant Profiling with Scanned Electrostatic Force Microscopes. *J. Vac. Sci. Technol. B* **1996**, *14*, 457–462.
22. Hudlet, S.; Saint Jean, M.; Roulet, B.; Berger, J.; Guthmann, C. Electrostatic Forces between Metallic Tip and Semiconductor Surfaces. *J. Appl. Phys.* **1995**, *77*, 3308–3314.
23. Wu, Y.; Shannon, M. A. AC Driving Amplitude Dependent Systematic Error in Scanning Kelvin Probe Microscope Measurements: Detection and Correction. *Rev. Sci. Instrum.* **2006**, *77*, 043711/1–9.
24. Nichols, J. A.; Gundlach, D. J.; Jackson, T. N. Potential Imaging of Pentacene Organic Thin-Film Transistors. *Appl. Phys. Lett.* **2003**, *83*, 2366–2368.
25. Müller, K.; Goryachko, A.; Burkov, Y.; Schwiertz, C.; Ratzke, M.; Köble, J.; Reif, J.; Schmeißer, D. Scanning Kelvin Probe and Photoemission Electron Microscopy of Organic Source-Drain Structures. *Synth. Met.* **2004**, *146*, 377–382.
26. Lei, C. H.; Das, A.; Elliot, M.; Macdonald, J. E. Quantitative Electrostatic Force Microscopy-Phase Measurements. *Nanotechnology* **2004**, *15*, 627–634.
27. Zerweck, U.; Loppacher, C.; Otto, T.; Grafström, S.; Eng, L. M. Accuracy and Resolution Limits of Kelvin Probe Force Microscopy. *Phys. Rev. B* **2005**, *71*, 125424/1–9.
28. Luo, Y.; Gustavo, F.; Henry, J.-Y.; Mathevet, F.; Lefloch, F.; Sanquer, M.; Rannou, P.; Grévin, B. Probing Local Electronic Transport at the Organic Single-Crystal/Dielectric Interface. *Adv. Mater.* **2007**, *19*, 2267–2273.
29. Puntambekar, K. P.; Pesavento, P. V.; Frisbie, C. D. Surface Potential Profiling and Contact Resistance Measurements on Operating Pentacene Thin-Film Transistors by Kelvin Probe Force Microscopy. *Appl. Phys. Lett.* **2003**, *83*, 5539–5541.
30. Smits, E. C. P.; Mathijssen, S. G. J.; Cölle, M.; Mank, A. J. G.; Bobbert, P. A.; Blom, P. W. M.; de Boer, B.; de Leeuw, D. M. Unified Description of Potential Profiles and Electrical Transport in Unipolar and Ambipolar Organic Field-Effect Transistors. *Phys. Rev. B* **2007**, *76*, 125202/1–6.
31. Silveira, W. R.; Marohn, J. A. Microscopic View of Charge Injection in an Organic Semiconductor. *Phys. Rev. Lett.* **2004**, *93*, 116104/1–4.
32. Bürgi, L.; Sirringhaus, H.; Friend, R. H. Noncontact Potentiometry of Polymer Field-Effect Transistors. *Appl. Phys. Lett.* **2002**, *80*, 2913–2915.